Title:

Why SARS-CoV-2 Omicron variant is milder? A single high-frequency mutation of structural envelope protein matters.

Authors:

Bingqing Xia[1,2,*], Yi wang[1,3], Xiaoyan pan[4], Xi Cheng[1,2], Hongying Ji[1], Xiaoli Zuo[1], Jia Li[1,2], Zhaobing Gao[1,2,*]

[1] CAS Key Laboratory of Receptor Research, Stake Key Laboratory of Drug Research, Shanghai Institute of Materia Medica, Chinese Academy of Sciences, 555 Zuchongzhi Road, Shanghai, 201203, China.

[2] University of Chinese Academy of Sciences, 19A Yuquan Road, Beijing, 100049, China.

[3] State Key Laboratory of Medical Neurobiology, Institutes of Brain Science, Fudan University, Shanghai 200032, China.

[4] State Key Laboratory of Virology, Wuhan Institute of Virology, Center for Biosafety Mega-Science, Chinese Academy of Sciences, Wuhan, 430071, China.

These authors contributed equally: Bingqing Xia, Yi wang

*Corresponding author. Email: zbgao@simm.ac.cn (Z.G.), xiabingqing@simm.ac.cn *(B.X.)*.

Abstract:

SARS-CoV-2 Omicron variant is highly transmissible and extensive morbidity, which has raised concerns for antiviral therapy. In addition, the molecular basis for the attenuated pathogenicity and replication capacity of Omicron remains elusive. Here, we report for the first time that a high-frequency mutation T9I on 2-E of SARS-CoV-2 variant Omicron forms a non-selective ion channel with abolished calcium permeability and reduced acid sensitivity compared to the WT channel. In addition, T9I caused less cell death and a weaker cytokine production. The channel property changes might be responsible for the Omicron variant releases less efficiently and induces a comparatively lower level of cell damage in the infected cells. Our study gives valuable insights into key features of the Omicron variant, further supporting 2-E is a promising drug target against SARS-CoV-2 and providing critical information for the COVID-19 treatment.

Mian Text：

Since November 2021, a new SARS-CoV-2 variant (B.1.1.529) emerged in South Africa and was designated as the fifth variant of concern (VOC), named as Omicron [1, 2]. Omicron variant is highly transmissible and extensive morbidity, which has raised concerns for antiviral therapy. Omicron has largest number (>30) of substitutions, deletions, or insertions with mutations frequency higher than 1% in the spike protein (S). Mutation studies in the spike RBD domain have provided a plausible explanation for altered transmissibility and antibody resistance [3-5]. Recent reports revealed Omicron variant induces a longer cycle for virus shed, attenuates replication capacity, and produces substantially attenuated lung pathology, indicating that the pathogenic ability of Omicron variant is indeed milder [6-8]. However, the molecular basis for the attenuated pathogenicity and replication capacity remains elusive. The envelope protein of SARS-CoV-2 (2-E) forms a homo-pentameric cation channel that is important for virus pathogenicity[9, 10]. It has been demonstrated that 2-E channel alone is sufficient to induce cell death, provoke cytokine storm and even cause acute respiratory distress syndrome (ARDS)-like damages *in vivo*. Its inhibitor exhibits excellent antiviral activity *in vivo*[9]. Therefore, we focus on the 2-E mutations of Omicron variant.

Three high quality E protein sequences of Omicron variants (B.1.1.529, BA1and BA2) in the CNCB database as of January 18th, 2022 (https://ngdc.cncb.ac.cn/ncov/) were comprehensively analyzed and a mutation 2-E^{T9I} (T9I) caught our attention. Compared with the original Wuhan reference strain, among more than one hundred identified 2-E mutations in Omicron variant, T9I shows a much higher frequency than the rest

mutations. In addition, the mutation probability of T9I in all statistical samples is higher than 99.5%. For the most common Omicron strain B.1.1.529, the mutation probability is 100% (Fig.1a, b). According to the solved NMR structure, T9 locates at the top of the transmembrane domain (TMD) of 2-E proteins [10]. The influence of T9I has not been studied yet completely.

First, we asked whether T9I still retains channel activity. We purified T9I protein and reconstituted the protein on Planar Lipid Bilayer (BLM) as previously described [9](Supplementary Fig.S1). The observed T9I-induced typical single-channel currents supported that T9I was able to form ion channels also as wild-type (WT) 2-E proteins [9]. However, the reversal potential of T9I channels was shifted to left, from 57 mV to 3 mV, under asymmetric KCl solutions. Similar reversal potential shifting was also detected in asymmetric NaCl solutions (Fig.1c.d, Supplementary Fig.S2). A reversal potential close to 0 mV suggests that T9I may have lost its selectivity to cations. To determine whether T9I can permeate chloride，the channel activity of T9I was further examined in asymmetric 50:500 mM choline chloride solutions. The quaternary ammonium choline is not permeable to most cation channels and thus is always used to detect anion permeability. As expected, outward currents were indeed observed when the holding voltage potentials were higher than the theoretical reversal potential for chloride (E_{rev}> 70 mV). Besides, WT channels are permeable to Ca^{2+}. As shown in Figure S2c, for WT channels, the frequent and continuous inward potassium currents in the asymmetric 50:500 mM (trans: cis) K^+ solutions indicated that the 2-E channels were incorporated into the membranes. The membrane potential was then changed to

78 +65 mV (K^+ reverse potential) to eliminate the K^+ currents. Intriguingly, outward step-
79 like signals appeared when 20 mM (final concentration) Ca^{2+} was added to the *trans*
80 side. When the Ca^{2+} concentration increased to 20 mM, the outward currents increased.
81 In contrast, under the identical conditions, T9I channels did not induce detectable
82 calcium currents (Supplementary Fig.S2c). These results revealed that T9I owns a
83 different ion selectivity and permeability from those of WT.

84 WT channels are pH sensitive [9]. The pH influences on T9I channels were evaluated on
85 a same channel using titration strategy. After the channels incorporated into the
86 membranes, HCl was titrated into either *cis* or *trans* side to alter the pH to 4 from 6.
87 Consistent to our previous results, reduction of pH, either in *cis* or *trans* side, induced
88 significant increase of amplitude and open probability of WT channels. In contrast, pH
89 reduction in *cis* side failed to increase the channel activity of T9I channels. Although
90 we didn't have direct evidences to explain how the threonine (T9) site is sensitive to
91 pH changes, the structure of 2-E channels supported the residues (Glu7 and Glu8)
92 around T9 were sensitive to pH change and their side chain carboxyl could be
93 deprotonated at neutral pH and protonated at acidic pH [10]. It is reported that SARS-
94 CoV-2 traffics to the lysosomes for egress by lysosome deacidification, instead of using
95 the conventional biosynthetic secretory pathway [11]. The E channels of coronavirus are
96 localized to intracellular organelles, including lysosome and Golgi apparatus [11, 12]. The
97 cellular localization and expression of WT and T9I were assessed using
98 immunocytochemistry and confocal microscopy. We found that both WT and T9I are
99 co-localized with the lysosomal marker LAMP (Fig.1g, supplementary Fig.S3). Given

100 the localization on lysosome, the influences of WT and T9I on the luminal pH of
101 lysosome were compared. Flow cytometric was used to analyze pH probe (pHluorin)
102 ratio. This pH probe consists of green fluorescent protein (GFP) pHluorin molecule
103 fused with lysosome-resident protein CD63. To generate a pH calibration curve, un-
104 transfected cells were subjected to treatment with buffers ranging from pH 5.5 to 7.5 in
105 the presence of the ionophores monensin and nigericin prior to flow analysis (Fig.1h,
106 i). Expression of WT channels robustly neutralized the lysosome pH, whereas T9I
107 channels exhibited less influences in luminal pH, which was consistent with our
108 electrophysiological results (Fig.1j). Therefore, the capability of deacidification of WT
109 channels in lysosomes was significantly impeded by the mutation T9I. Based on above,
110 whether the weakened capability of deacidification hampers virus releasing was
111 examined. We transfected the Vero E6 cells with WT or T9I plasmids at day 1, then the
112 cells were infected with SARS-CoV-2 virus at day 2. As determined by qRT-PCR, pre-
113 expression of mutant T9I significantly attenuated viral loadings compared with WT
114 (Fig.1k). It was logic to deduce that some exogenous T9I subunits would co-assemble
115 with the WT subunits originated from the virus and form heteromultimers with impaired
116 pH sensitivity, resulting in less deacidification of lysosomes and less SARS-CoV-2
117 virus releasing.

118 Finally, the channel activity of the 2-E protein is a determinant of virulence. We used
119 Annexin V/PI staining and CCK8 assays to evaluate the cell lethality of T9I in Vero E6
120 cells. We found that although the expression level of T9I was far exceeding the
121 expression level of WT (Fig. 1 l), it caused similar cell death as WT did (Fig. 1 m,

122 supplementary Fig.S4a). Similarly, in the mouse macrophage cell line (RAW264.7), a
123 very highegreater expression of T9I induced a comparable increase of inflammatory
124 cytokines as WT did (Fig. 1n, Supplementary Fig.S4b). The correlation between the
125 cell lethality and the expression level was further compared. As shown in Figure 1o, in
126 comparison with WT, the killing cells capability of T9I was dropped around 150 times
127 as well as the cytokines production. Notably, according to another latest study, the 2-E
128 expression in Omicron variant was decreased approximately 3-fold, which may further
129 suppress the virulence of Omicron variants [6]. How much the weakened capabilities of
130 killing cells and inducing cytokine production confer the milder clinical symptoms of
131 Omicron warrant further investigation.

132 Overall, as SARS-CoV-2 infections are progressing, there are chances that virus
133 accumulates new mutations. Among existed antiviral targets, different from spike
134 protein, RNA-dependent RNA polymerase (Rdrp) and 3CL pro, which mediate virus
135 entry, protein cleavage and viral replication, respectively, the envelope protein (2-E)
136 majorly participating in the virus releasing [13-15]. Here we report for the first time that a
137 high-frequency 2-E mutation T9I of SARS-CoV-2 variant Omicron forms a non-
138 selective ion channel with abolished calcium permeability and reduced acid sensitivity
139 compared to WT channels. In addition, T9I caused less cell death and a weaker cytokine
140 production (Fig.1p). The channel property changes might be responsible for the
141 Omicron variant releases less efficiently and induces a comparatively lower level of
142 cell damage in the infected cells. According to 2-E NMR structures, although T9I is not
143 located in the pore domain of the channel, it may alter the channel configuration via

interacting with the amino acids at positions L12 and T11 (Supplementary Fig.S5). Our study provides valuable insights into key features of the Omicron variant and critical information for the COVID-19 treatment.

Acknowledgement:

We are grateful to the National Science Fund of Distinguished Young Scholars (81825021), Fund of Youth Innovation Promotion Association (2019285), the National Natural Science Foundation of China (81773707, 92169202), the National Key Research and Development Program of China (2020YFC0842000), the National Key Laboratory Program of China (LG202101-01-04), Fund of National Science and Technology Major Project (2018ZX09711002-002-006) and the Hubei Science and Technology Project (2020FCA003) for financial support.

Author contributions:

Z. G., and B. X. conceived designed the project. Z. G., J. L., and B. X designed the experiments; Y. W. and B. X. performed the electrophysiological recordings; B. X. carried out the cell-based assays; P. X. carried out the virus assays in vitro; Y. W purified the proteins; H.Y. analyzed the sequence; all authors analyzed and discussed the data. Z. G., B. X. wrote the manuscript. All authors read and approved the manuscript.

Reference:

1 Karim SSA, Karim QA. Omicron SARS-CoV-2 variant: a new chapter in the COVID-19 pandemic. *Lancet (London, England)* 2021; **398**:2126-2128.

2 Organization WH. Classification of Omicron (B.1.1.529): SARS-CoV-2 Variant of Concern.<*https://wwwwhoint/news/item/26-11-2021-classification-of-omicron (b11529) -sars-cov-2-variant-of-concern*>.

3 Cao Y, Wang J, Jian F *et al.* Omicron escapes the majority of existing SARS-CoV-2 neutralizing antibodies. *Nature* 2021.

4 Cele S, Jackson L, Khoury DS *et al.* Omicron extensively but incompletely escapes Pfizer BNT162b2 neutralization. *Nature* 2021.

5 Bojkova D, Widera M, Ciesek S, Wass MN, Michaelis M, Cinatl J, Jr. Reduced interferon antagonism but similar drug sensitivity in Omicron variant compared to Delta variant of SARS-CoV-2 isolates. *Cell research* 2022:1-3.

6 Shuai H, Chan JF, Hu B *et al.* Attenuated replication and pathogenicity of SARS-CoV-2 B.1.1.529 Omicron. *Nature* 2022.

7 Halfmann PJ, Iida S, Iwatsuki-Horimoto K *et al.* SARS-CoV-2 Omicron virus causes attenuated disease in mice and hamsters. *Nature* 2022.

8 Torjesen I. Covid-19: Peak of viral shedding is later with omicron variant, Japanese data suggest. *BMJ (Clinical research ed)* 2022; **376**:o89.

9 Xia B, Shen X, He Y *et al.* SARS-CoV-2 envelope protein causes acute respiratory distress syndrome (ARDS)-like pathological damages and constitutes an antiviral target. *Cell research* 2021; **31**:847-860.

10 Mandala VS, McKay MJ, Shcherbakov AA, Dregni AJ, Kolocouris A, Hong M. Structure and drug binding of the SARS-CoV-2 envelope protein transmembrane domain in lipid bilayers. *Nature structural & molecular biology* 2020; **27**:1202-1208.

11 Ghosh S, Dellibovi-Ragheb TA, Kerviel A *et al.* β-Coronaviruses Use Lysosomes for Egress Instead of the Biosynthetic Secretory Pathway. *Cell* 2020; **183**:1520-1535.e1514.

12 Westerbeck JW, Machamer CE. The Infectious Bronchitis Coronavirus Envelope Protein Alters Golgi pH To Protect the Spike Protein and Promote the Release of Infectious Virus. *Journal of virology* 2019; **93**.

13 Yin W, Mao C, Luan X *et al.* Structural basis for inhibition of the RNA-dependent RNA polymerase from SARS-CoV-2 by remdesivir. *Science (New York, NY)* 2020; **368**:1499-1504.

14 Jin Z, Du X, Xu Y *et al.* Structure of M(pro) from SARS-CoV-2 and discovery of its inhibitors. *Nature* 2020; **582**:289-293.

15 Liu L, Wang P, Nair MS *et al.* Potent neutralizing antibodies against multiple epitopes on SARS-CoV-2 spike. *Nature* 2020; **584**:450-456.

Figure:

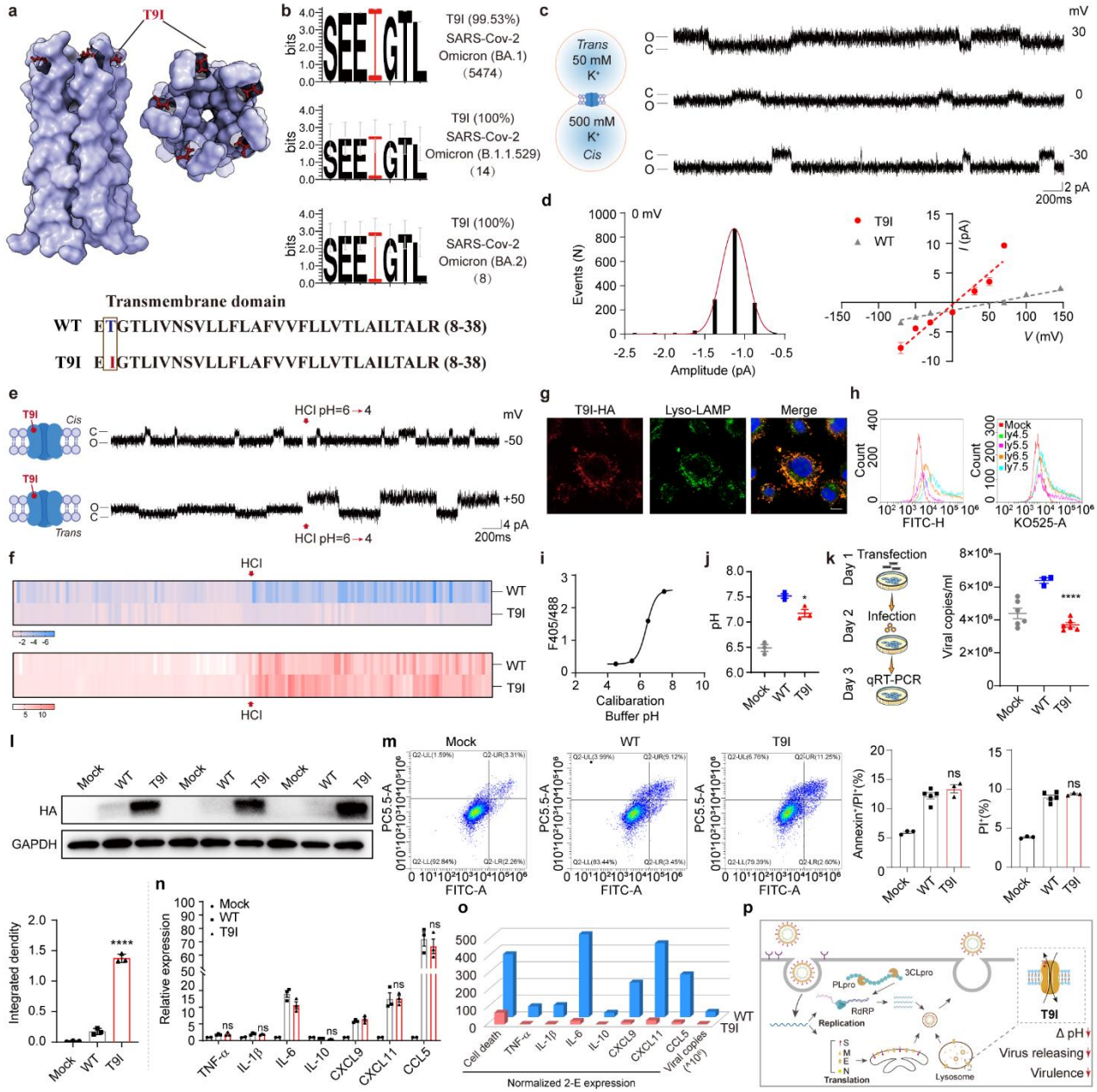

Fig.1 The envelope protein mutation T9I of SARS-CoV-2 Omicron variant shows less pathogenicity and weakens virus production.

a, Structure of the 2-E TM domain [10]. Illustration of the amino-acid sequence of SARS-CoV-2 E (8-38) and the indicated mutants. Threonine residues (T) are marked as blue and the T >I mutants are marked as red. **b,** 2-E protein amino-acid sequence logo of

211 SARS-CoV-2 Omicron variant. The I9 residues are marked as red. 2-E protein
212 sequences were downloaded from China National Center for Bioinformation (CNCB)
213 using the "Lineage Browse" option. Logos were generated using the WebLogo 3.7.4
214 online tool. **c,** Single-channel current recording of T9I after reconstitution in lipid
215 bilayers with PC/PS = 3:2 lipids at indicated potentials and solutions (Left). **d,** Left, all-
216 point current histograms for the trace in **c** (0 mV) ("C" means Closed; "O" means Open).
217 Right, *I-V* curves of T9I in the solutions of **c** ($n \geq 3$). **e**, Single-channel current recording
218 in 500 :500 mM KCl solutions via proton titration result in different pH (*cis* or *trans*).
219 Red arrow represents titration of HCl. **f,** The heat map shows the transition of the
220 currents from panel **e** under proton titration. **g,** Cell immunofluorescence of T9I (Red)
221 and lysosome marker LAMP (Green). T9I is co-localized with lysosome. **h-j,** Lyso-pH
222 indicator was used to assess the pH of the lysosome via flow cytometry. Flow cytometry
223 pattern of the cells in buffers of known pH and contained ionophores to equilibrate the
224 extracellular and lysosome luminal pH (**h**). Calibration curves were generated from data
225 like those illustrated in h (**i**). **j,** The pH value of Vero E6 cells lysosome transfected with
226 WT, T9I or Mock. **k.** Flow chart of the experiment (Left), the virus copies in supernatant
227 determined by qRT-PCR assay (Right). MOI of SARS-CoV-2 for infection was 0.01. **l,**
228 Protein expression levels of WT and T9I in Vero E6 cells after transfection (Up). The
229 histogram shows the quantization of the result (Bottom). **m,** Flow cytometry pattern of
230 Vero E6 cells transfected with WT or T9I plasmids. Right, flow cytometry analysis of
231 Propidium iodide (PI) and Annexin V stained Vero E6 cells. **n,** Serum cytokine levels
232 at 24 h after transfection with WT, T9I or Mock detected by RT-qPCR. **o,** The relative

activity of WT, T9I in pH regulation, cell virulence, channel conductance and viral copies normalized to the expression levels. **p,** Life cycle pattern diagram of SARS-CoV-2 Omicron variant. T9I on envelope protein (2-E) of SARS-CoV-2 variant Omicron forms a non-selective ion channel with weakened pathogenicity and virus production. Experiments were independently performed thrice and similar results were obtained. One set of reprehensive data is shown here ($n \geqslant 3$). $^{*}p < 0.05$; $^{**}p < 0.01$; $^{***}p < 0.001$; unpaired Student's t test. All error bars are SEM.

241 **Method:**

242 **Plasmids and mutagenesis**

243 Wild type SARS-CoV-2-E sequences were synthesized by the Beijing Genomics
244 Institute (BGI, China). The mutants 2-E^{T9I} sequence was generated by site-directed
245 mutagenesis and confirmed by sequencing (BGI, China). Vector pET28a was used for
246 protein purification; vector pcDNA5 and pcDNA3.1 were used for cell survival assay
247 and cell imaging.

248 **Cell culture and treatment**

249 Vero E6 and Raw 264.7 cells were grown in 90% DMEM basal medium (Gibco, USA)
250 supplemented with 10% fetal bovine serum (Gibco, USA) at 37°C under 5% CO_2.

251 **Planar lipid bilayers recording**

252 According to our previous methods, the purified protein 2-E^{WT} or 2-E^{T9I} were
253 incorporated into lipid bilayers to test their functionality. The lipid bilayers were
254 prepared by PC: PS= 3: 2 (Avanti Polar Lipids, USA). Proteins were added in *cis* side
255 and the solution was 50:500 mM (*trans*: *cis*) KCl or others, all solutions were buffered
256 by 5mM HEPES, pH 6.35. Membrane currents were recorded by headstage connected
257 with amplifier BC-535 (Warner Instruments, USA), filtered at 1–2 kHz and digitized
258 by Axon Digidata 1440A (Molecular Devices, USA). The recording frequency was 10
259 kHz. The data were processed using pClamp 10.2 software (Molecular Devices, US).
260 The single-channel conductance was determined by fitting to Gaussian functions (bin
261 width = 0.25 pA). Opening time less than 0.5–1.5 ms was ignored to avoid noise

262 interference. The equilibrium potential was calculated using Goldman–Hodgkin–Katz

263 flux equation:

264 $$E_m = \frac{RT}{F} \ln \left(\frac{P_{Na^+}[Na^+]_{out} + P_{Cl^-}[Cl^-]_{in} + P_{K^+}[K^+]_{out}}{P_{Na^+}[Na^+]_{in} + P_{Cl^-}[Cl^-]_{out} + P_{K^+}[K^+]_{in}}\right)$$

265

266 **Cell viability and cytotoxicity assay**

267 Cell viability was measured by the CCK-8 kit (40203ES60, Yeason, China) according

268 to the manufacturer's instructions. The absorbance was measure at 450 nm with Thermo

269 Scientific Microplate Reader (Thermo Fisher Scientific Inc., USA).

270 **Western blotting and antibodies**

271 Proteins were resolved in 12% SDS-PAGE, transferred to PVDF membranes (GE,

272 USA). The PVDF membranes were incubated with primary antibodies against HA-Tag

273 (C29F4) (3724, CST, USA) or GAPDH (30201ES20, Yeasen, China), then incubated

274 with second antibodies against IgG (Yeasen, China).

275 **Flow cytometry of cell death**

276 After treatment, cells were detached, collected by centrifugation and resuspended in 1×

277 binding buffer containing 100 μg/mL propidium iodide (PI) and Annexin V-FITC (1:20,

278 V13242, Life, USA) and incubated at room temperature for 15 min in the dark.

279 Subsequently, samples were added 400 μL of 1× binding buffer and kept on ice. Cells

280 were analyzed by flow cytometry using BD FACSCALIBUR 4 (BD COMPANY, USA).

281 The percentages of differently labeled cells were calculated by FlowJo 7.6.

282 **Immunofluorescence microscopy.**

283 Vero E6 cells were seeded as 1×10^4 cells per well in coverslips on chamber slides
284 (Thermo Fisher Scientific Inc., USA) overnight. Cells were transfected with WT or T9I
285 with lysosome marker (LAMP1,). After transfection for 24 h, cells were washed with
286 phosphate-buffered saline (PBS) and fixed in 4% paraformaldehyde for 10 min at room
287 temperature. Then the cells were permeabilized in 0.5% Triton X-100 in PBS for 3
288 min. The coverslips were washed twice with PBS and incubated with primary antibody
289 in 1% bovine serum albumin (BSA) (36101ES25, Yeasen, China) for 2 h at room
290 temperature. Anti-HA (HT301-01, Trans, China) and rabbit anti-LAMP (55273-1-AP,
291 Proteintech, USA) were used to incubate the cells at a 1:1,000 dilution. Then, second
292 antibodies FITC-AffiniPure Goat Anti-Rabbit IgG (33107ES60, Yeasen, China) and
293 Cy3-AffiniPure Goat Anti-Mouse IgG (33208ES60, Yeasen, China)were used to
294 incubate the cells at a 1:1,000 dilution. Images were captured using the Leica TCS-SP8
295 STED system with 100× oil objective.

296 **Virus loading and quantitative real-time PCR (qRT-PCR) analysis**

297 SARS-CoV-2 (nCoV-2019BetaCoV/Wuhan/WIV04/2019) was preserved at Wuhan
298 institute of virology, Chinese Academy of Sciences. It was propagated and titrated with
299 Vero E6 cells, and its associated operations were performed in a biosafety level 3 (BSL-
300 3) facility. Cell supernatants RNA was isolated with MiniBEST Viral RNA/DNA
301 Extraction Kit (Takara, Japan) as described in the instruction, and cDNA was
302 transcribed with PrimeScript^{TM} RT reagent Kit with gDNA Eraser (Takara, Japan). In

303 detail, 50 μL supernatant were collected for RNA isolation with a MiniBEST Viral
304 RNA/DNA Extraction Kit Ver.5.0 (Takara, AK41820A), and the total RNA was eluted
305 with 30 μL RNase-free water. cDNA was transcribed from 3 μL total RNA in 20 μL
306 reaction system with PrimeScriptTM RT reagent Kit with gDNA Eraser (Takara,
307 AK71648A). Viral copies were quantified from 1 μL template viral cDNA by a standard
308 curve method on ABI 7500 (Takara TB Green Premix Ex Taq II, AK81975A) with a
309 pair of primers targeting S gene. The forward primer (5'-3') is:
310 CAATGGTTTAACAGGCACAGG; the reverse primer (5'-3') is:
311 CTCAAGTGTCTGTGGATCACG.

312 **Determination of lysosome pH**

313 Vero cells were transfected with Lyso-pHluorin (addgene,70113) and 2-E plasmid.
314 After transfection, cells were trypsinzed and washed with Live Cell Imaging Solution
315 (LCIS). Then, replaced LCIS with cellular pH calibration Buffers containing 10 μM
316 Valinomycin and Nigericin (Intracellular pH Calibration Buffer Kit, P35379, Themo,
317 USA) and incubate at 37°C for at least 5 minutes. At last, cells were analyzed via Flow
318 cytometry with excited at 405 nm and 488 nm, and the emission signals were collected
319 with detection filters at 500 to 550 nm and 515 to 545 nm, respectively. Flow cytometric
320 data were collected and quantified using CytoExpert 2.4 software.

321 **Homology modeling**

322 The solid-state NMR structure of SARS-CoV-2 envelope protein (PDB code: 7k3g)
323 [(2020) Nat Struct Mol Biol 27: 1202-1208] was used to as the template to build

homology models of the mutant envelope protein. This solid-state data yield to ten lowest-energy structures. These ten structures were employed to construct ten homology models of the mutant envelope protein using Modeller [A. Sali, T.L. Blundell, Comparative protein modelling by satisfaction of spatial restraints, J Mol Biol 234 (1993) 779-815. 10.1006/jmbi.1993.1626.]. The models with the lowest root mean square deviations from their template structures were selected.

Statistics

All measurements were derived from distinct samples. Statistics were performed in GraphPad Prism. Statistical significance was determined by one-way ANOVA and two-way ANOVA followed by pairwise Student's t-test with Tukey's or Sidak's correction. Two-tailed unpaired Student's t test was performed if only two conditions were compared. Data in the text is presented as Mean ± SEM. Adjusted P values are reported in the figures.

Supplementary figure：

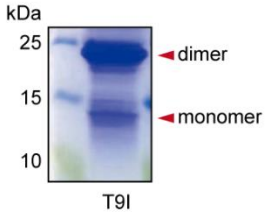

Supplementary information, Fig. S1 Purification of T9I proteins. Purification of full-length 2-E^{T9I} protein with Ni-NTA affinity chromatography. 15% SDS-PAGE gel with coomassie blue staining.

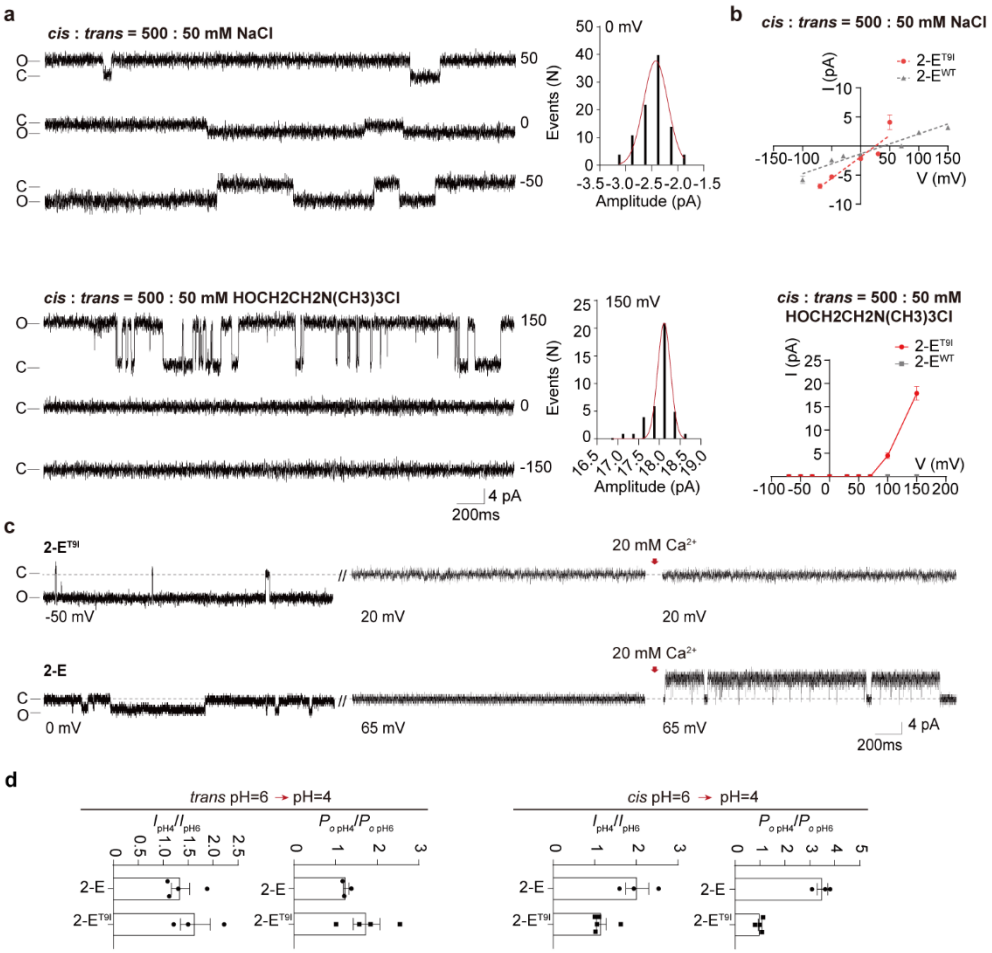

Supplementary information, Fig. S2 Electrophysiological property of T9I.

a. Single-channel current recording of T9I after reconstitution in lipid bilayers with

PC/PS = 3:2 lipids at indicated potentials and solutions. Protein (5–50 ng/mL) was added to the cis side. All-point current histograms for the left trace (0, 150mV) ("C" means Closed; "O" means Open). **b.** *I-V* curves of T9I in indicated solutions (n ≥ 3). **c.** Pure Ca^{2+} currents recording in 50 :500 mM KCl solutions (*trans*: *cis*) via calcium titration as indicated concentrations, red arrow represents titration of $CaCl_2$. **d.** Amplitude (*I*) and open probability (P_o) of channel current at pH 4 were normalized to channel current at pH 6 of both sides (n ≥ 3).

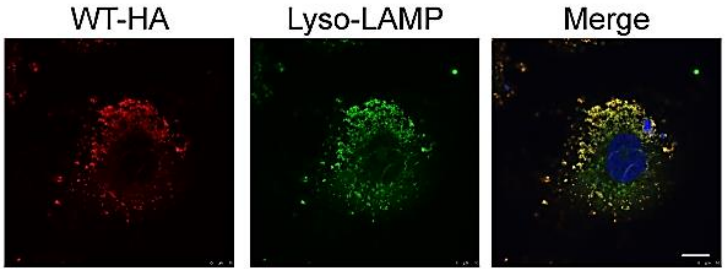

Supplementary information, Fig. S3 Wild type envelope protein (E) is co-localized with lysosome. Cell immunofluorescence of WT (Red) and lysosome marker (Green). Scale bar,10 μM.

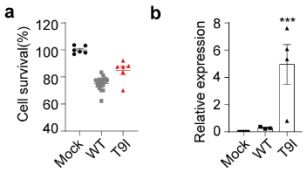

Supplementary information, Fig. S4 Cell viability of Vero E6 cells after transfection with 2-E plasmids and expression level of after transfection with WT andT9I.

362 **a.** Cell viability of Vero E6 cells after transfection with WT, T9I or Vector (Mock) at

363 24 h. **b.** Expression level of 2-E after transfection with WT, T9I or Mock in Raw

364 264.7 cells detected by RT-qPCR.

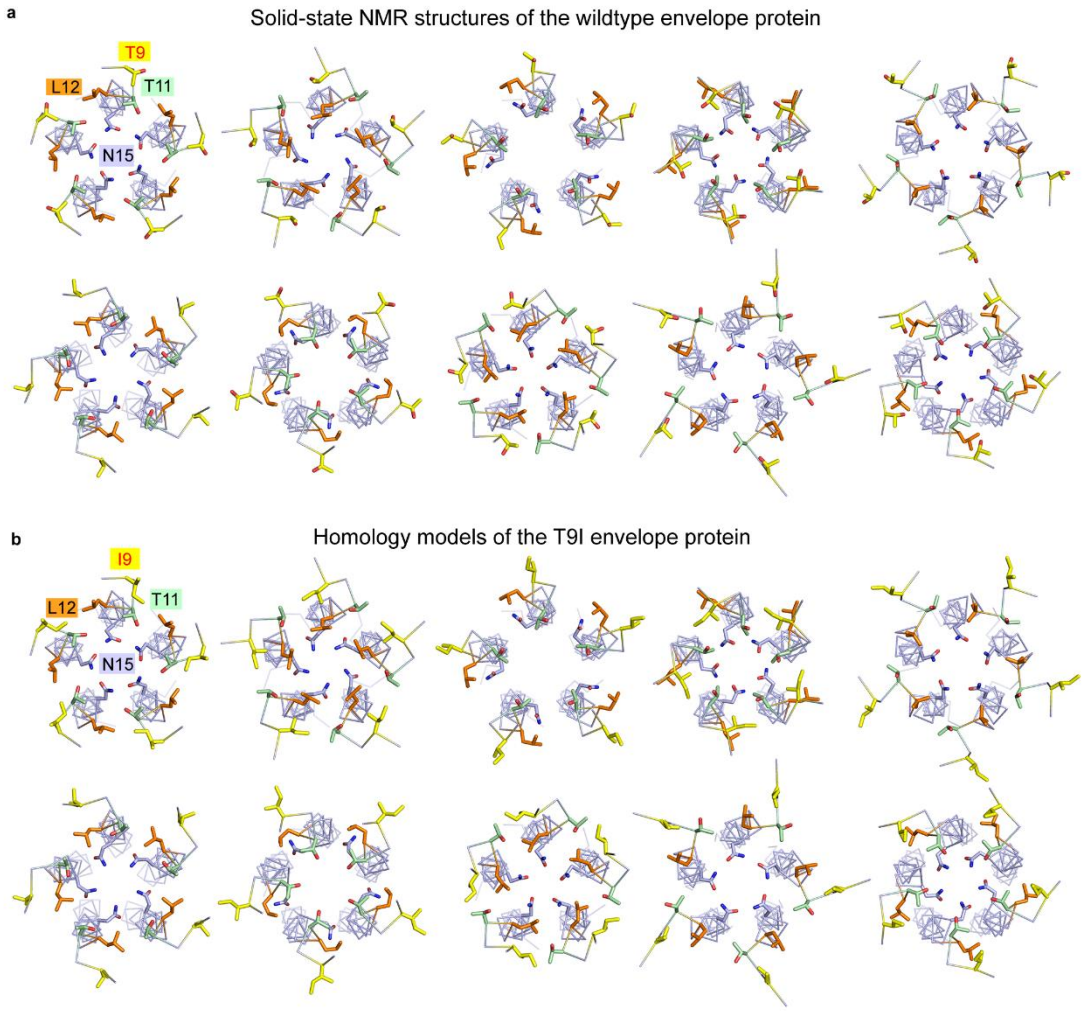

365

366 **Supplementary information, Fig. S5 Structure of WT and T9I.**

367 **a**, Top view of ten lowest-energy solid-state NMR structures of wildtype SARS-CoV-2

368 E protein (PDB code: 7k3g). Three N-terminal residues T9, T11, L12 and a pore-lining

369 residue N15 are shown as sticks (T9 in *yellow*, T11 in *green*, L12 in *orange*, N15 in

370 *light blue*). The protein is shown as ribbon. **b,** Top view of ten homology models of2-

371 E^{T9I}, which built based on the solid-state NMR structures of wildtype SARS-CoV-2

envelope protein (PDB code: 7k3g). Three N-terminal residues I9, T11, L12 and a pore-lining residue N15 are shown as sticks (I9 in *yellow*, T11 in *green*, L12 in *orange*, N15 in *light blue*).